Applied Catalysis B: Environmental 340 (2024) 123196

Contents lists available at ScienceDirect

Applied Catalysis B: Environmental

journal homepage: www.elsevier.com/locate/apcatb

Ultrafast electron transfer from CdS quantum dots to atomically-dispersed Pt for enhanced H_2 evolution and value-added chemical synthesis

Xianglin Xiang [a], Liuyang Zhang [b,*], Cheng Luo [a], Jianjun Zhang [b], Bei Cheng [a], Guijie Liang [c,*], Zhenyi Zhang [d], Jiaguo Yu [b,*]

[a] State Key Laboratory of Advanced Technology for Materials Synthesis and Processing, Wuhan University of Technology, Wuhan 430070, PR China
[b] Laboratory of Solar Fuel, Faculty of Materials Science and Chemistry, China University of Geosciences, Wuhan 430078, PR China
[c] Hubei Key Laboratory of Low Dimensional Arts and Science, Hubei University of Arts and Science, Xiangyang 441053, PR China
[d] Key Laboratory of New Energy and Rare Earth Resource Utilization of State Ethnic Affairs Commission; Key Laboratory of Photosensitive Materials and Devices of Liaoning Province, School of Physics and Materials Engineering, Dalian Minzu University, 18 Liaohe West Road, Dalian 116600, Liaoning, China

ARTICLE INFO

Keywords:
Artificial photosynthesis
Organic building blocks
Quantum dots
Atomically dispersed cocatalysts

ABSTRACT

Photocatalytic hydrogen production is enchanting in solar energy utilization. And mechanism elucidation in interfacial electron transfer rate is a prerequisite for performance improvement. Herein, atomically dispersed Pt-modified CdS quantum dots (Pt-CdS QDs), prepared by a facile one-step in-situ deposited method, are used as a prototype. Benefiting from the maximized utilization of Pt cocatalyst as well as the strong electronic metal-support interaction, ultrafast electron transfer from CdS to Pt (~1.7 ps) is achieved, as revealed by femto-second transient absorption spectra. The optimal sample simultaneously realizes photocatalytic hydrogen evolution coupled with selective oxidation of 2-thiophene methanol (TM) into 2-thiophenecarboxaldehyde (TD). Specifically, it exhibits an enhanced H_2-evolution rate, which is 70-fold higher than pristine CdS QDs. Moreover, a TM conversion rate of 95.3 % with a TD selectivity of 87.2 % is reached after 4 h. This work will provide some guidance for the design of photocatalytic systems with efficient interfacial electron transfer.

1. Introduction

Solar energy utilization for the production of renewable chemical energy occupies a prominent place [1–5]. Recently, the coproduction of H_2 fuel and value-added chemicals by dual-functional photocatalytic systems becomes intriguing [6–10]. Firstly, conventional organic synthesis is tedious and requires harsh reaction conditions while the photocatalytic approach is under mild conditions [11]. Secondly, the concurrent utilization of photoinduced holes and electrons in a one-step photoredox cycle meets the sustainability goal. However, the selectivity of targeted chemicals and the H_2 production activity is difficult to balance. Thus, the photocatalysts, the most critical part, should be appropriately selected and finely tuned. Compared to common large nanoparticle photocatalysts, semiconductor quantum dots (QDs) have been recognized as promising alternatives due to their unique ability in light absorption, abundant surface active sites, effective carrier separation, and adjustable bandgaps [12–15]. Pitifully, single QD suffers from rapid recombination of photogenerated carriers, leading to reduced photocatalytic performance [16]. Fortunately, cocatalyst modification is effective in facilitating charge separation and transfer [17–26]. Nevertheless, because of the extremely small size and the complex ligands of QDs, it is challenging to load the cocatalysts on the surface of QDs and meanwhile ensure their intimate contact and rapid charge transfer [27]. Typically, cocatalysts can be introduced onto the surface of QDs via a facile electrostatic self-assembly approach or with the assistance of complex organic ligands. However, most of these systems exhibit moderate H_2-production activity and undesired byproducts due to the weak interaction between QDs and cocatalysts, which hampers the electron transfer from QDs to the reducing active site.

Recently, owing to the strong "electronic metal-support interactions (EMSI)", the loading of atomically dispersed noble metals onto semiconductor supports has become a hot spot for various catalytic reactions [28–30]. EMSI was first proposed by Campbell to describe the observed orbital rehybridization and charge transfer at the metal–support interface, resulting in the realignment of molecular energy levels [31,32]. In these systems, the noble metal atoms can be directly bonded to the supports via strong chemical bonds, preventing the aggregation of noble metal atoms [33]. Meanwhile, the strong EMSI can modulate the

* Corresponding authors.
E-mail addresses: zhangliuyang@cug.edu.cn (L. Zhang), guijie-liang@hbuas.edu.cn (G. Liang), yujiaguo93@cug.edu.cn (J. Yu).

https://doi.org/10.1016/j.apcatb.2023.123196
Received 18 April 2023; Received in revised form 3 August 2023; Accepted 19 August 2023
Available online 21 August 2023
0926-3373/© 2023 Elsevier B.V. All rights reserved.

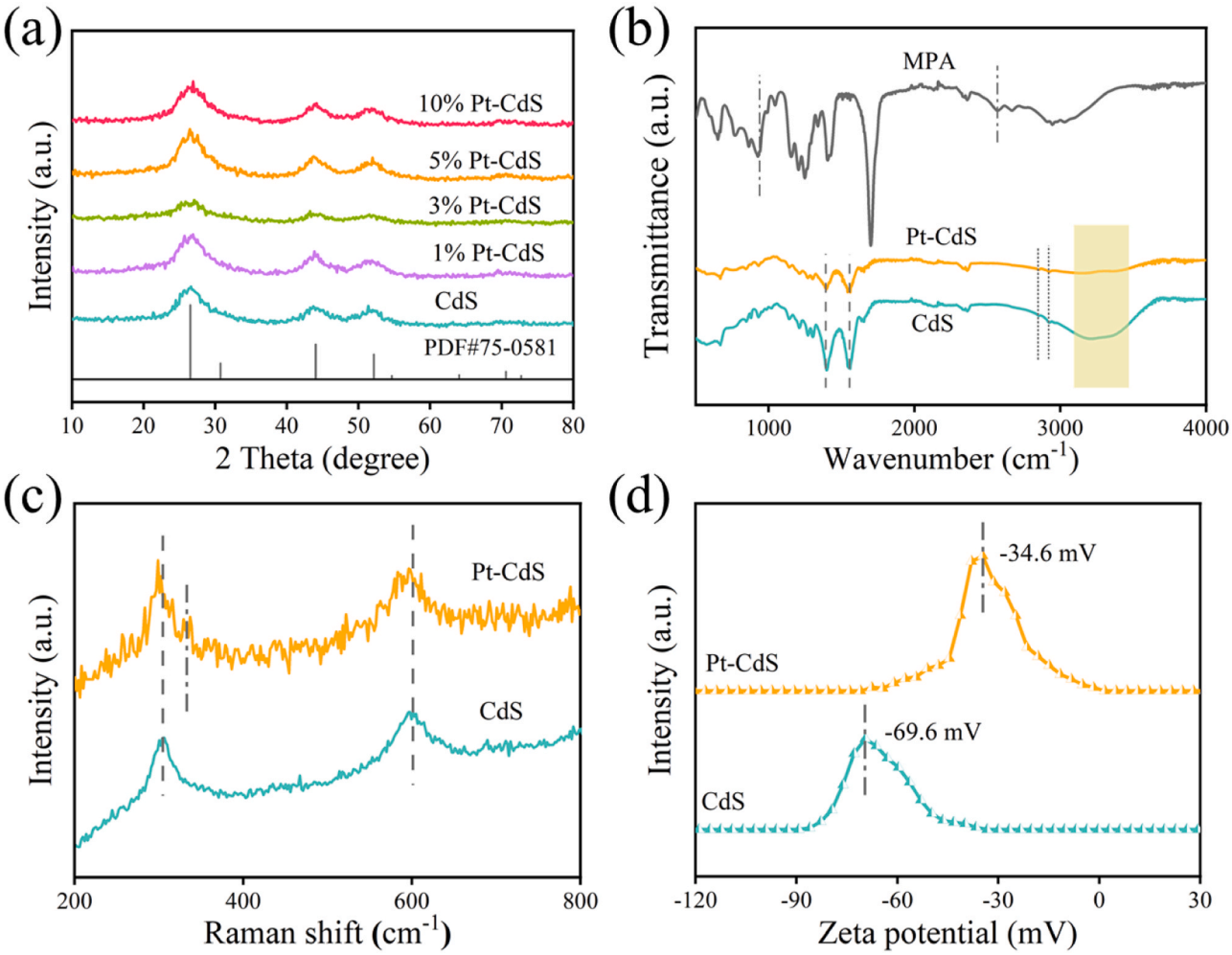

Fig. 1. (a) XRD spectra of CdS and *x*Pt-CdS. (b) FT-IR spectra of CdS, Pt-CdS, and MPA. (c) Raman spectra of CdS and Pt-CdS. (d) Zeta potential of Pt-CdS and CdS at pH 7.

electron transfer of metal atoms and supports, leading to the spatial charge separation of metal atoms and supports. Hence, the loading of noble metal cocatalysts onto QDs with strong EMSI is suitable for the bifunctional system. Moreover, it can maximize the added value by boosting the photocatalytic activity for both the oxidation and reduction sides. In addition, platinum (Pt) is considered to be one of the most effective hydrogen evolution cocatalysts for its large work function, strong electron capture ability, and low hydrogen evolution overpotentials [34–36].

Herein, 2-thiophenecarboxaldehyde (TD) is selected as an important platform compound, which can be derived from the oxidation of 2-thiophene methanol (TM). As an organosulfur compound, 2-thiophenecarboxaldehyde (TD) and its derivations are important organic building blocks, which can introduce thiophene groups, in the preparation of pharmaceuticals, pesticides, dyes, and other chemical reagents. The atomically dispersed Pt-modified CdS QDs (Pt-CdS QDs) with strong EMSI were prepared through a facile one-pot solvothermal method followed by a ligand exchange process. Through this one-pot method, Pt can be directly deposited on the surface of CdS with atomic dispersion, which ensures intimate contact between CdS and Pt. This synthetic protocol guarantees ultrafast electron transport (1.7 ps), as disclosed by the result of femtosecond transient absorption (fs-TA) spectra. And this also greatly enhances the photocatalytic performance. Particularly, under optimal conditions, Pt-CdS QDs exhibit an enhanced H_2-production rate of 2.12 mmol h^{-1} g^{-1}, which is 70-fold higher than pristine CdS QDs. After photoreactions for 4 h, a TM conversion rate of 95.3 % and a TD selectivity of 87.2 % are obtained, which exceeds some previous results (Table S1). Based on density functional theory (DFT) calculations, the reaction path is proposed. This research will open up new possibilities for the design of QD-based high-performance photocatalytic systems.

2. Experimental section

2.1. Synthesis of Pt-modified CdS quantum dots (Pt-CdS QDs)

Pt-CdS QDs were prepared using a solvent-thermal approach. Typically, The Cd-precursor solution was prepared by heating a solution containing CdO (3.5 mmol), oleic acid (OA, 7 mL), and 1-octadecene (ODE, 7 mL) to 230 °C in an N_2 atmosphere. Subsequently, the S-OAm solution formed by dissolving sulfur powders (3.5 mmol) into oleylamine (OAm, 5 mL) was transferred into the Cd-precursor solution to produce CdS QDs. Then, a set amount of chloroplatinic acid was dissolved into OAm (5 mL) to form a clear Pt (IV)-OAm solution. Pt-CdS QDs were obtained by adding the Pt-precursor solution into a solution containing CdS QDs at 230 °C. The obtained samples were denoted as *x*Pt-CdS, where *x* is the theoretical mass ratio of Pt to CdS. The optimal content of Pt-CdS (5 %) was denoted as Pt-CdS. Subsequently, the synthesized Pt-CdS QDs were transformed into water-soluble Pt-CdS QDs using a ligand exchange process assisted by mercaptopropionic acid (MPA) following our previous literature [16].

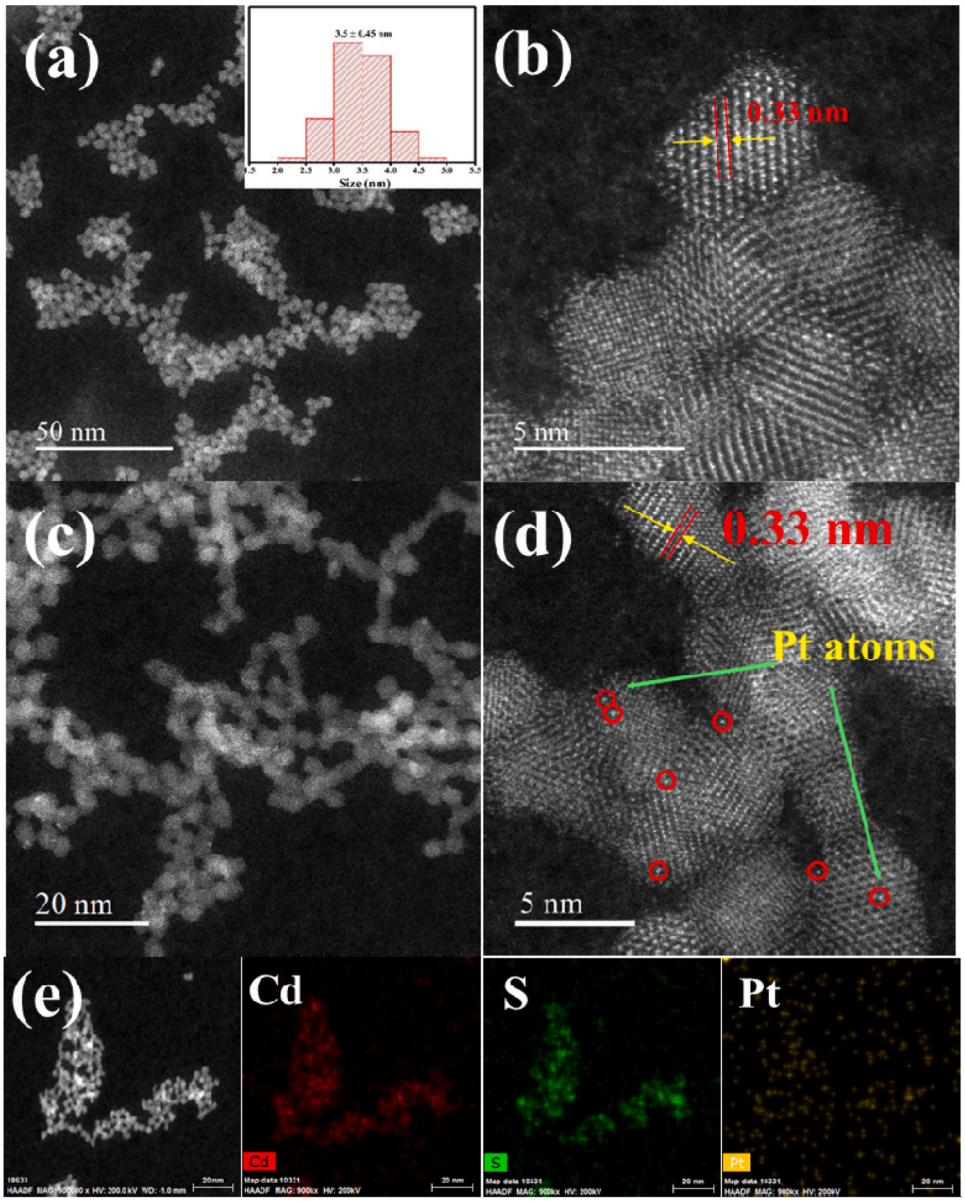

Fig. 2. (a) Low and (b) high magnification HAADF STEM images of CdS. The inset of (a) is the particle-size histogram. (c) Low and (d) high magnification HAADF STEM images of Pt-CdS. (e) EDS mapping images of Cd, S, and Pt of Pt-CdS.

2.2. Synthesis of pure CdS QDs

The procedure for the preparation of pure CdS QDs was the same as that for Pt-CdS QDs, except for the absence of chloroplatinic acid.

3. Results and discussion

Different from the previous method in constructing Pt on CdS quantum dots, a facile one-pot solvothermal method was used. Unlike the self-assembly method, it avoids the complex surface modification of CdS and Pt species. Also, it prevents the aggregation of Pt species and ensures the tight anchoring of Pt on the surface of CdS. Due to the small size of CdS QDs and the intimate contact between CdS and Pt, ultrafast electron transport from CdS to Pt is achieved.

3.1. Morphology and structure

To verify the crystal phases of the prepared samples, X-ray diffraction (XRD) measurements were performed. The XRD spectrum of pristine CdS (Fig. 1**a**) exhibits three main peaks at 52.0°, 43.9°, and 26.5°, which can be assigned to (331), (220), and (111) facets of cubic CdS, respectively [37,38]. No shift of these three peaks in *x*Pt-CdS samples was observed, indicating that Pt mainly exists on the surface rather than in the lattice of CdS. Due to the large atomic mass and relatively inert inherent properties of Pt, and relatively stable crystal structure of CdS QDs, Pt cannot diffuse into the lattice of CdS QDs to form a solid solution or alloy, resulting in surface bonding of Pt to CdS QDs. Moreover, no characteristic peaks for Pt species were detected, which may be ascribed to its low content or poor crystallization. Notably, these diffraction peaks are relatively broad, which is ascribed to the small crystalline size of CdS QDs [39].

Surface ligands are essential for the stability of quantum dots. To study the surface ligand of the samples, Fourier transform infrared (FTIR) spectroscopy analysis was conducted. As for the spectra of Pt-CdS and CdS (Fig. 1**b**), a broad peak appears at ~3300 cm^{-1}, assigned to the O−H vibration of MPA[40]. Two peaks at 2919 and 2851 cm^{-1} can be attributed to the vibrational signals of C−H of MPA [41]. Two strong bands at 1543 and 1391 cm^{-1} are attributed to the symmetric stretching

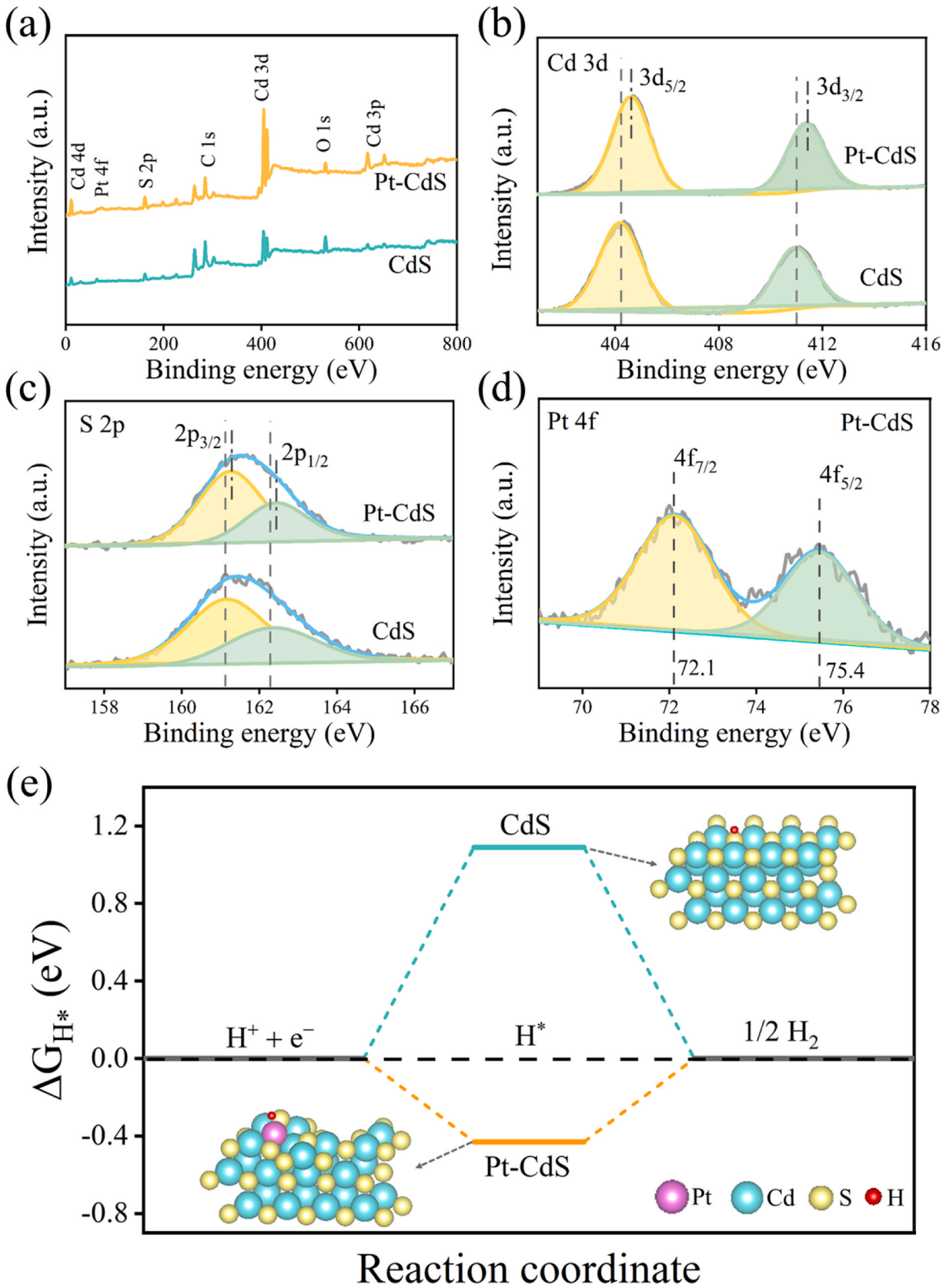

Fig. 3. (a) XPS survey spectrum and high-resolution XPS spectra of (b) Cd 3d, (c) S 2p, and (d) Pt 4 f of Pt-CdS and CdS. (e) The calculated ΔG_{H^*} values of Pt-CdS and CdS.

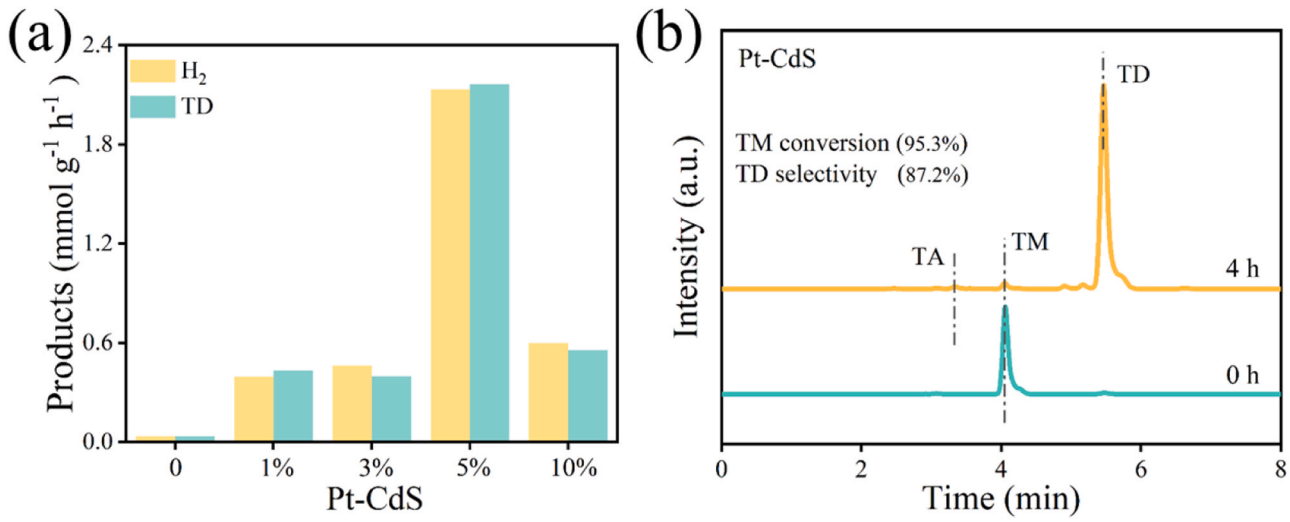

Fig. 4. (a) Yields of H_2 and TD after photocatalytic hydrogen evolution coupled with TM oxidation over CdS and *x*Pt-CdS ($x = 1$, 3, 5, and 10) for 1 h. (b) HPLC spectra of the photocatalytic oxidation of TM over Pt-CdS for 4 h.

and stretching vibration of carboxylate anions, respectively [42,43]. This implies that the carboxyl group has turned into its anion during the ligand exchange process. The disappearance of the peaks at 2570 and 940 cm^{-1}, ascribed to the vibrations of H−S, in both samples, is due to the cleavage of H−S bond and the formation of Cd−S bond [44]. The FTIR spectra reveal that the MPA ligand is successfully bonded to the surface of CdS through Cd–S bond. No bands of Pt species were detected in the Pt-CdS spectrum, which can be attributed to the weak infrared response and the low content of Pt species. Raman spectra were collected to study the existence of Pt in Pt-CdS. As shown in Fig. 1**c,** two bands at 303 and 600 cm^{-1} are the characteristic Raman signals of CdS [45]. In the spectrum of Pt-CdS QDs, these two peaks are slightly shifted towards low wavenumbers, implying an intimate contact between Pt and CdS. A new band at 333 cm^{-1} emerges in the spectrum of Pt-CdS, which can be assigned to the formation of Pt−S [46,47]. Fig. 1**d** presents the Zeta potential of the prepared samples at pH 7. The Zeta potential of Pt-CdS and CdS are − 34.6 and − 69.6 mV, respectively. The positive shift of the Zeta potential for Pt-CdS again implies the successful loading of Pt, altering the surface properties of CdS QDs.

To study the morphology and microstructure of the samples, transmission electron microscopy (TEM) analyses were carried out. The high-angle annular dark-field (HAADF) STEM image (Fig. 2**a**) of CdS exhibits numerous quasi-spherical geometries with diameters of approximately 3.5 ± 0.45 nm. High magnification HAADF STEM image (Fig. 2**b**) confirms that CdS is highly crystalized with a lattice spacing of 0.33 nm, which is assigned to (111) facet of CdS [48]. Pt-CdS shows a similar morphology and microstructure with CdS (Fig. 2**c,d**). This indicates that Pt mainly exists on the surface rather than in the lattice of CdS QDs. The bright contrast spots are ascribed to the Pt atoms. No Pt clusters and nanoparticles were detected in the TEM images of Pt-CdS, indicating the atomic dispersion of Pt. The energy dispersive X-ray spectrometer (EDS) mapping images of Pt-CdS (shown in Fig. 2**e**) disclose the uniform distribution of Cd, S, and Pt in the selected region. This implies that Pt species are uniformly distributed on CdS. Due to the strong EMSI effect, Pt can be tightly bonded to the surface of CdS to achieve atomic dispersion.

X-ray photoelectron spectroscopy (XPS) measurements were performed to determine the surface chemical state of the prepared samples. As shown in Fig. 3**a**, Cd, S, O, and C elements are all detected in the survey spectrum of CdS. O is mainly derived from MPA ligands. C mainly originates from the MPA. Additionally, the Pt element is observed in the XPS spectrum of Pt-CdS, indicating the successful loading of Pt on CdS. As for pristine CdS, two peaks emerge at 411.0 and 404.3 eV in the Cd 3d spectrum (Fig. 3**b**), which are the signals of Cd $3d_{3/2}$ and Cd $3d_{5/2}$, respectively [49–51]. Two fitted peaks at 162.3 and 161.1 eV correspond to S $2p_{1/2}$ and $2p_{3/2}$, respectively (Fig. 3**c**) [52–54]. Compared to those of CdS, the binding energies of S and Cd for Pt-CdS both shift towards high energy. This not only indicates that there is a strong EMSI between Pt and CdS but also proves that an electron flow from CdS to Pt is successfully achieved. Two peaks at 75.4 and 72.1 eV are assigned to 4 $f_{5/2}$ and Pt 4 $f_{7/2}$, respectively (Fig. 3**d**) [55]. This indicates that Pt mainly exists in Pt-CdS through a Pt−S bond with a + 2 oxidation state. The actual content of Pt measured by ICP-AES in Pt-CdS is 2.44 wt%.

The light absorption properties of the samples were analyzed using ultraviolet-visible (UV–vis) absorption spectroscopy measurements. Bare CdS QDs show an obvious absorption edge at 450 nm (Fig. S1), which corresponds to a band gap of 2.75 eV. Compared with bare CdS QDs, Pt-CdS QDs show no enhancement of light absorption at the wavelength of 400–800 nm. This indicates that Pt mainly exists in the form of atomic dispersion rather than metal clusters or nanoparticles which will exhibit a surface plasmon resonance effect [56–58].

To accurately measure the band position of CdS QDs, the ultra-violet photoelectron spectroscopy (UPS) spectra (Fig. S2a-**b**) were collected. The calculated valence band (VB) position of CdS is 1.72 eV [59]. According to the band gap of CdS (2.75 eV), the CB position of CdS is −1.03 eV. The hydrogen evolution overpotentials of the samples were measured by linear sweep voltammetry (LSV) measurements. The hydrogen evolution overpotentials of Pt-CdS and CdS are −0.35 V and −0.50 V, respectively (Fig. S3). The lower hydrogen evolution overpotential of Pt-CdS implies higher hydrogen evolution activity. The free energy of hydrogen atom adsorption (ΔG_{H^*}) values of the samples are shown in Fig. 3**e.** The absolute ΔG_{H^*} ($|\Delta G_{H^*}|$) value of CdS is 1.1 eV, which is higher than that of Pt-CdS (0.43 eV). The near-zero $|\Delta G_{H^*}|$ of Pt-CdS suggests that the loading of Pt will result in higher H_2 activity.

The contact potential difference (CPD) tests were used to further investigate the electron transfer between CdS and Pt. As shown in Fig. S4, the CPD values of Pt nanoparticles (NPs), Pt-CdS, and CdS are 0.60, 0.12, and −0.37 V, respectively. Therefore, the work functions of Pt NPs, Pt-CdS, and CdS are calculated to be 4.85, 4.37, and 3.88 eV, respectively (Supporting Information eq. 2). Therefore, Pt has a much lower Fermi energy level than CdS, which induces a strong driving force for the electron transfer from CdS to Pt, facilitating the separation efficiency of photoinduced carriers.

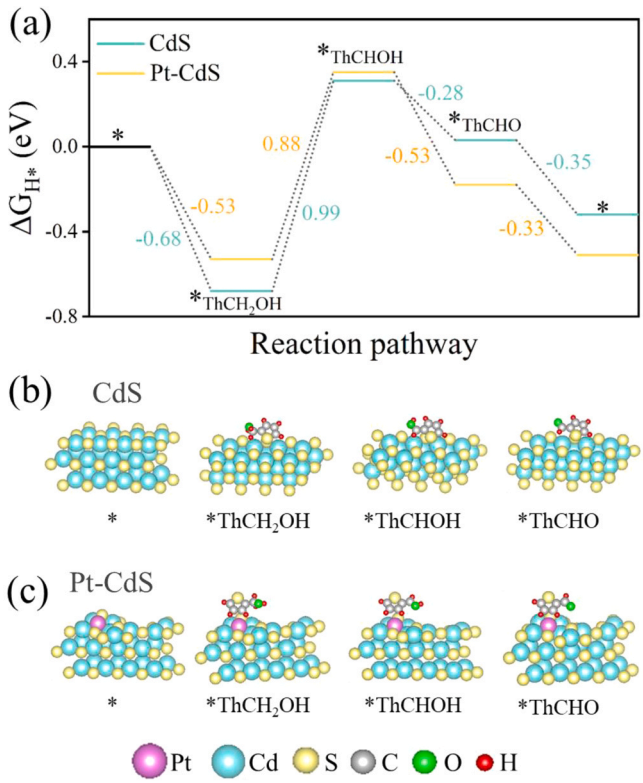

Fig. 5. (a) DFT calculations of energy barriers for different intermediates of TM oxidation on CdS and Pt-CdS, respectively. The simulated adsorption and transformation of TM over (b) CdS and (c) Pt-CdS.

3.2. Photocatalytic hydrogen production coupled with organic synthesis activity

The photocatalytic experiments of the samples were conducted using TM as an oxidation reactant. Fig. 4**a** demonstrates that pristine CdS exhibits a relatively low photocatalytic performance (0.03 mmol h^{-1} g^{-1}) for the rapid recombination of photoinduced carriers. After the loading of 1 wt% of Pt as cocatalysts, the photocatalytic activity is greatly improved (0.39 mmol h^{-1} g^{-1}). With the increase in Pt content, the H_2-production performance of the samples is further enhanced. The photocatalytic hydrogen evolution rate of the optimal sample (5 %Pt-CdS) is 2.12 mmol h^{-1} g^{-1}. This is 70-fold higher than that of bare CdS. Further increasing the content of Pt leads to performance deterioration. This could be ascribed to that the excessive amount of Pt could act as recombination centers, preventing the separation of photogenerated carriers. Furthermore, excess platinum will promote the backward reaction from H_2 to H_2O. Moreover, the ratio of TD to H_2 is close to 1:1. This indicates that the oxidation of TM to TD and hydrogen evolution consume equal amounts of photogenerated holes and electrons. Therefore, this system makes full utilization of photoinduced carriers.

To track the concentration changes of TM and its oxidation products, high-performance liquid chromatography (HPLC) analyses were carried out. As shown in Fig. S5, three peaks at 4.04、5.46, and 3.26 min are assigned to the commercial TM, TD, and 2-thiophenecarboxylic acid (TA), respectively. By contrast, only a trace of TA is detected and almost all the TM was converted (Fig. 4**b**), implying the high selectivity of the oxidation of TM to TD. Combined with quantitative analysis by HPLC (Fig. S6, S7, and **S8**), a TM conversion rate of 95.3 % with TD selectivity of 87.2 % is reached through this system.

Nuclear magnetic resonance hydrogen spectrum (H NMR) and nuclear magnetic resonance carbon spectrum (C NMR) experiments were carried out to identify the oxidation products. As shown in Fig. S9, 4 peaks at 7.24, 7.93, 8.00, and 9.93 in the H NMR spectrum of the product correspond to the standard signals of TD (inset). As shown in Figs. S10, 5 peaks at 129.1, 136.1, 137.9, 144.0, and 184.2 in the C NMR spectrum of the liquid product are indexed to the standard signals of TD (inset). The H NMR and C NMR spectra also prove that the oxidation product is TD.

To track the source of hydrogen in the photocatalytic process, the GC–MS spectra of the photocatalytic H_2-evolution gas of Pt-CdS were performed. The signals at 4, 3, and 2 correspond to D_2, HD, and H_2, respectively (Fig. S11). The main product is D_2. Only a small amount of HD is detected. The production of H_2 is negligible. These imply that the hydrogen is mainly derived from water rather than the dehydrogenation of TM.

To disclose the reaction pathway over CdS and Pt-CdS, DFT calculations were carried out. The oxidation of TM ($ThCH_2OH$) to TD involves two consecutive dehydrogenation steps. The first dehydrogenation step may produce oxygen or carbon center radicals (Fig. S12, S13). The energy barriers of the oxygen and carbon center radical processes of CdS and Pt-CdS indicate that the energy barrier of the latter is lower than that of the former. This suggests that the hydrogen atom of the C−H bond is broken down prior to the O−H bond. As shown in Fig. 5**a-c**, both the rate-determining step of CdS and Pt-CdS is the breakage of C−H. And the energy barrier over Pt-CdS (0.88 eV) is lower than that over bare CdS

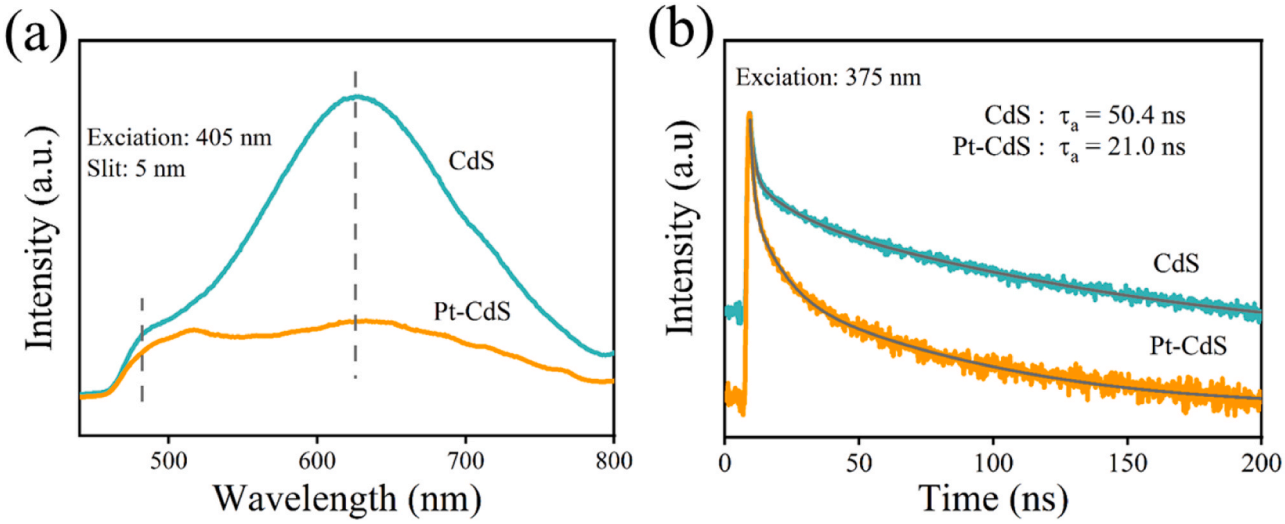

Fig. 6. (a) PL and (b) TRPL spectra of Pt-CdS and CdS.

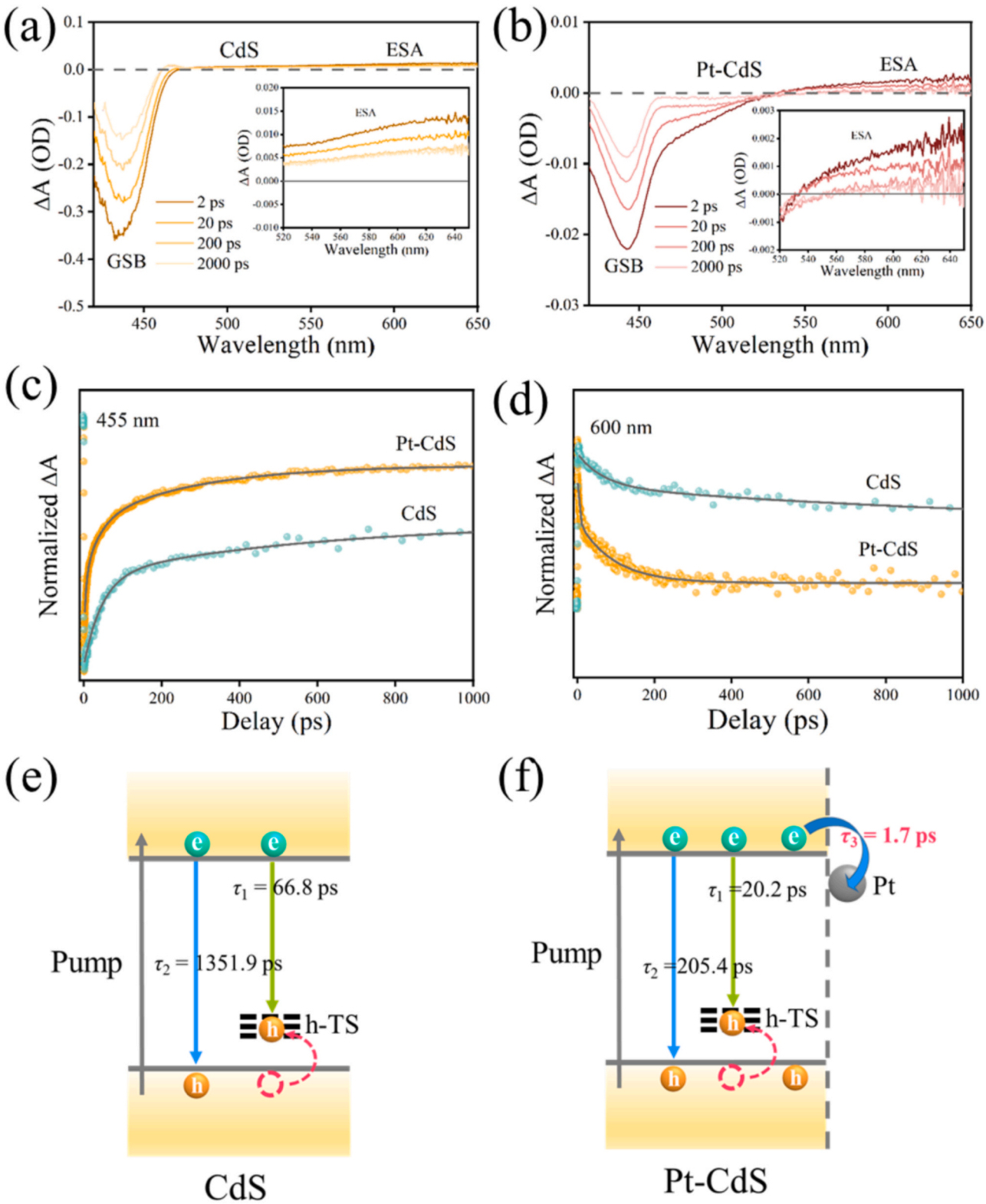

Fig. 7. The fs-TA spectra of (a) CdS and (b) Pt-CdS at given delay times using a 400 nm pump laser. Normalized fs-TA kinetics at (c) 455 nm and (d) 600 nm for CdS and Pt-CdS. The schematic of electron quenching in (e) CdS and (f) Pt-CdS.

(0.99 eV), revealing that the introduction of Pt is feasible in promoting the oxidation thermodynamically.

Henceforth, a plausible mechanism for photocatalytic H_2 evolution integrated with selective oxidation of TM over Pt-CdS is proposed. Initially, TM is adsorbed on CdS. The electrons of CdS are excited to CB, while holes remain in VB after light irradiation. The electrons at the CB of CdS rapidly transfer to Pt for hydrogen production, while the holes are transferred to the surface of CdS for the selective oxidation of TM. The selective oxidation of TM to TD is a two-step reaction. Firstly, TM is attacked by a hole to generate a carbon-centered radical and an H^+. Subsequently, the carbon radical reacts with another hole to form TD and releases another H^+. Then, TD is desorbed from the surface of CdS.

Table 1
Fitting results of fs-TA kinetics of CdS and Pt-CdS probed at 455 nm and 600 nm.

Samples	τ_1 (ps)	A_1 (%)	τ_2 (ps)	A_2 (%)	τ_3 (ps)	A_3 (%)	τ_a (ps)
455 nm CdS	66.8	3.2	1351.9	96.8			1309.9
455 nm Pt-CdS	20.2	8.8	205.4	89.0	1.7	2.2	184.5
600 nm CdS	46.4	11.1	586.1	88.8			525.8
600 nm Pt-CdS	6.2	6.7	130.8	93.3			122.5

The H^+ ions derived from the dehydrogenation reaction of TM are released into the water. Finally, H^+ ions from water are reduced to H_2. The photogenerated holes of Pt-CdS have a weak oxidation ability (1.72 V vs. normal hydrogen electrode, NHE), making it difficult to further oxidize TD into TA (2.15 V vs. NHE Fig. S14). Thus, TD can not be further oxidated to TA by Pt-CdS.

To measure the stability of the photocatalyst, the cycling test was performed. As shown in Fig. S15, the photocatalytic performance show no obvious degradation after 5 consecutive reaction cycles. The XRD patterns (Fig. S16) exhibit that the crystal structure of Pt-CdS photocatalyst does not change after the photocatalytic reactions. The XPS spectra (Fig. S17a-**d**) reveal that the chemical states of Pt-CdS catalyst do not alter after photocatalytic reactions. In addition, Pt species still exist in the form of + 2 oxidation states rather than reduced to platinum metals after photocatalytic reactions. This implies that Pt is tightly anchored onto the surface of CdS.

3.3. Photocatalytic electron transfer kinetics

The separation efficiency of photoinduced carriers of the samples was investigated using steady-state fluorescence spectra (PL) and time-resolved fluorescence spectra (TRPL). For pristine CdS, two peaks at 625 and 483 nm (Fig. 6**a**) correspond to the hole trapping states (h-TS) and band edge emission of CdS, respectively [60,61]. The peaks of Pt-CdS are much weaker than those of CdS, indicating an enhanced separation efficiency of photoinduced electrons and holes [62]. Fig. 6**b** exhibits the TRPL spectra of the samples. The delay curves of the samples can be fitted by a double-exponential equation (Table S2). τ_1 and τ_2 represent the radiative and non-radiative decay processes of the samples, respectively [63]. Both the values of τ_1, τ_2, and τ_a of Pt-CdS are much smaller than those of CdS, implying an enhanced separation efficiency of photoinduced carriers [64]. In addition, Pt-CdS show an enhanced transient photocurrent density, demonstrating the high separation efficiency of photoexcited carriers at the Pt/CdS interface (Fig. S18a). The electrochemical impedance spectra (EIS) show that Pt-CdS exhibits a relatively smaller semicircle radius than CdS, indicating its lower charge transfer resistance and thus higher separation and transfer efficiencies of photogenerated carriers (Fig. S18b).

To further analyze the dynamics of the photoinduced carriers of the samples, femtosecond transient absorption (fs-TA) spectroscopy measurements were conducted. Fig. 7**a and** Fig. 7**b** are the fs-TA spectra of CdS and Pt-CdS at given delay times, respectively. The positive peak at 530–650 nm and negative peak at ~440 nm are the excited-state absorption (ESA) and ground-state bleach (GSB) signals of CdS, respectively [65,66]. As previously reported, the GSB signal of CdS is merely related to the electron dynamics due to the high degeneracy of the hole levels and the high effective mass of the holes [37,67]. The ESA signal of CdS at 530−650 nm is assigned to the dynamics of trapped holes [68]. The lifetime of the photogenerated electrons and holes was obtained by fitting the fs-TA kinetics (Fig. 7**c,d**) probed at 455 and 600 nm, respectively, and the corresponding fitting results are shown in Table 1. As for the electron dynamics of CdS, the τ_1 (66.8 ps) is ascribed to the recombination of electrons in the conduction band minimum (CBM) and the holes at trap states, and τ_2 (1351.9 ps) is attributed to the band-to-band recombination [69]. In addition, three lifetimes are obtained for the electron dynamics of Pt-CdS. The τ_1 (20.2 ps) and τ_2 of Pt-CdS (205.4 ps) correspond to the same electron dynamics in single CdS, while the τ_3 (1.7 ps) is assigned to the electron transfer from the CBM of CdS to Pt cocatalysts (Fig. 7**e,f**). The τ_3 is much shorter than that of previous reports [70,71]. The ultrashort τ_3 indicates that Pt effectively facilitates the electron extraction of CdS for photocatalytic hydrogen evolution. In addition, the τ_1 and τ_2 of Pt-CdS are much shorter than those of CdS, suggesting that the electron separation and transfer of Pt-CdS is more efficient. Consequently, the average electron lifetime of Pt-CdS (184.5 ps) is shorter than that of CdS (1309.9 ps). Furthermore, the average hole lifetimes of CdS and Pt-CdS are 525 ps and 122 ps, respectively. The average lifetimes of both electrons and holes in Pt-CdS are shorter than those in CdS. This implies that the holes and electrons in Pt-CdS are effectively separated and transferred once they are excited.

4. Conclusions

In summary, atomically dispersed Pt-CdS QDs are successfully synthesized through a facile solvothermal method. CPD analysis indicates that a strong driving force for the transfer of electrons from CdS to Pt is established. In addition, the fs-TA spectra disclose the ultrafast electron transfer from CdS to Pt, facilitating the extraction of electrons from CdS to Pt. Moreover, DFT calculations reveal the reaction pathway of TM oxidation. Hence, a high photocatalytic performance of hydrogen evolution coupled with TM oxidation is achieved. It exhibits an enhanced H_2-production rate of 2.12 mmol h^{-1} g^{-1}, which is 70-fold higher than pristine CdS QDs. After photoreactions for 4 h, a TM conversion rate of 95.3 % and a TD selectivity of 87.2 % are obtained. This research will create new possibilities for the design of efficient photocatalytic systems.

CRediT authorship contribution statement

Xianglin Xiang: Conceptualization, Methodology, Data curation, Writing – original draft. **Liuyang Zhang:** Formal analysis, Writing – review & editing. **Jianjun Zhang:** Formal analysis. **Bei Cheng:** Data curation, Funding acquisition. **Guijie Liang:** Data curation. **Zhenyi Zhang**:Software. **Jiaguo Yu:** Supervision, Funding acquisition, Writing – review & editing.

Declaration of Competing Interest

The authors declare that they have no known competing financial interests or personal relationships that could have appeared to influence the work reported in this paper.

Data availability

Data will be made available on request.

Acknowledgments

This work is supported by the National Key Research and Development Program of China (2022YFB3803600 and 2022YFE0115900), the National Natural Science Foundation of China (Nos. 22278383, 52073223, 22278324, 51932007, 22238009, 22261142666 and U1905215) and the Natural Science Foundation of Hubei Province of China (2022CFA001).

Appendix A. Supporting information

Supplementary data associated with this article can be found in the online version at doi:10.1016/j.apcatb.2023.123196.

References

[1] Y.W. Liu, W.X. Yang, Q.L. Chen, D.A. Cullen, Z.X. Xie, T.Q. Lian, Pt particle size affects both the charge separation and water reduction efficiencies of CdS-Pt nanorod photocatalysts for light driven H_2 generation, J. Am. Chem. Soc. 144 (2022) 2705–2715.

[2] W.C. Wang, Y. Tao, J.C. Fan, Z.P. Yan, H. Shang, D.L. Phillips, M. Chen, G.S. Li, Fullerene-graphene acceptor drives ultrafast carrier dynamics for sustainable CdS photocatalytic hydrogen evolution, Adv. Funct. Mater. 32 (2022), 2201357.

[3] X.B. Li, Z.K. Xin, S.G. Xia, X.Y. Gao, C.H. Tung, L.Z. Wu, Semiconductor nanocrystals for small molecule activation via artificial photosynthesis, Chem. Soc. Rev. 49 (2020) 9028–9056.

[4] S. Wageh, A.A. Al-Ghamdi, O.A. Al-Hartomy, M.F. Alotaibi, L. Wang, CdS/polymer S-scheme H_2-production photocatalyst and its in-situ irradiated electron transfer mechanism, Chin. J. Catal. 43 (2022) 586–588.

[5] L. Yuan, M.Y. Qi, Z.R. Tang, Y.J. Xu, Coupling strategy for CO_2 valorization integrated with organic synthesis by heterogeneous photocatalysis, Angew. Chem. Int. Ed. 60 (2021) 21150–21172.

[6] M.-Y. Qi, M. Conte, M. Anpo, Z.-R. Tang, Y.-J. Xu, Cooperative coupling of oxidative organic synthesis and hydrogen production over semiconductor-based photocatalysts, Chem. Rev. 121 (2021) 13051–13085.

[7] C.Y. Toe, C. Tsounis, J.J. Zhang, H. Masood, D. Gunawan, J. Scott, R. Amal, Advancing photoreforming of organics: highlights on photocatalyst and system designs for selective oxidation reactions, Energy Environ. Sci. 14 (2021) 1140–1175.

[8] M.-Y. Qi, Z.-R. Tang, Y.-J. Xu, Near field scattering optical model-based catalyst design for artificial photoredox transformation, ACS Catal. 13 (2023) 3971–3982.

[9] Y.-H. Li, Z.-R. Tang, Y.-J. Xu, Multifunctional graphene-based composite photocatalysts oriented by multifaced roles of graphene in photocatalysis, Chin. J. Catal. 43 (2022) 708–730.

[10] M.-Y. Qi, Q. Lin, Z.-R. Tang, Y.-J. Xu, Photoredox coupling of benzyl alcohol oxidation with CO_2 reduction over CdS/TiO_2 heterostructure under visible light irradiation, Appl. Catal. B 307 (2022), 121158.

[11] J.-Y. Li, Y.-H. Li, M.-Y. Qi, Q. Lin, Z.-R. Tang, Y.-J. Xu, Selective organic transformations over cadmium sulfide-based photocatalysts, ACS Catal. 10 (2020) 6262–6280.

[12] X.-B. Li, C.-H. Tung, L.-Z. Wu, Semiconducting quantum dots for artificial photosynthesis, Nat. Rev. Chem. 2 (2018) 160–173.

[13] H. Zhu, Y. Yang, T. Lian, Multiexciton annihilation and dissociation in quantum confined semiconductor nanocrystals, Acc. Chem. Res. 46 (2013) 1270–1279.

[14] M. Jouyandeh, S.S.M. Khadem, S. Habibzadeh, A. Esmaeili, O. Abida, V. Vatanpour, N. Rabiee, M. Bagherzadeh, S. Iravani, M.R. Saeb, R.S. Varma, Quantum dots for photocatalysis: synthesis and environmental applications, Green. Chem. 23 (2021) 4931–4954.

[15] X.B. Fan, S. Yu, X. Wang, Z.J. Li, F. Zhan, J.X. Li, Y.J. Gao, A.D. Xia, Y. Tao, X.B. Li, L.P. Zhang, C.H. Tung, L.Z. Wu, Susceptible surface sulfide regulates catalytic activity of CdSe quantum dots for hydrogen photogeneration, Adv. Mater. 31 (2019), 1804872.

[16] X. Xiang, B. Zhu, B. Cheng, J. Yu, H. Lv, Enhanced photocatalytic H_2-production activity of CdS quantum dots using Sn^{2+} as cocatalyst under visible light irradiation, Small 16 (2020), 2001024.

[17] Z. Wang, C. Li, K. Domen, Recent developments in heterogeneous photocatalysts for solar-driven overall water splitting, Chem. Soc. Rev. 48 (2019) 2109–2125.

[18] S. Cao, Y. Chen, H. Wang, J. Chen, X.H. Shi, H.M. Li, P. Cheng, X.F. Liu, M. Liu, L. Y. Piao, Ultrasmall CoP nanoparticles as efficient cocatalysts for photocatalytic formic acid dehydrogenation, Joule 2 (2018) 549–557.

[19] X. Xiang, L. Wang, J. Zhang, B. Cheng, J. Yu, W. Macyk, Cadmium chalcogenide (CdS, CdSe, CdTe) quantum dots for solar-to-fuel conversion, Adv. Photonics Res. 3 (2022), 2200065.

[20] J. Zhang, Y. Le, Y. Zhang, Bifunctional photocatalyst for H_2 production and high-value product synthesis, J. Mater. Sci. Technol. 142 (2023) 121–123.

[21] S. Wageh, A. A, Al-Ghamdi, Q. Xu, Core-Shell $Au@NiS_{1+x}$ cocatalyst for excellent TiO_2 photocatalytic H_2 production, Acta Phys. -Chim. Sin. 38 (2022), 2202001.

[22] J. Xu, D. Gao, H. Yu, P. Wang, B. Zhu, L. Wang, J. Fan, Palladium-copper nanodot as novel H_2-evolution cocatalyst: Optimizing interfacial hydrogen desorption for highly efficient photocatalytic activity, Chin. J. Catal. 43 (2022) 215–225.

[23] M.-Y. Qi, M. Conte, Z.-R. Tang, Y.-J. Xu, Engineering semiconductor quantum dots for selectivity switch on high-performance heterogeneous coupling photosynthesis, ACS Nano 16 (2022) 17444–17453.

[24] C.-L. Tan, M.-Y. Qi, Z.-R. Tang, Y.-J. Xu, Cocatalyst decorated $ZnIn_2S_4$ composites for cooperative alcohol conversion and H_2 evolution, Appl. Catal. B 298 (2021), 120541.

[25] M.-Y. Qi, Y.-H. Li, M. Anpo, Z.-R. Tang, Y.-J. Xu, Efficient photoredox-mediated C–C coupling organic synthesis and hydrogen production over engineered semiconductor quantum dots, ACS Catal. 10 (2020) 14327–14335.

[26] J.-Y. Li, M.-Y. Qi, Y.-J. Xu, Efficient splitting of alcohols into hydrogen and C–C coupled products over ultrathin Ni-doped $ZnIn_2S_4$ nanosheet photocatalyst, Chin. J. Catal. 43 (2022) 1084–1091.

[27] X.-B. Li, Y.-J. Gao, Y. Wang, F. Zhan, X.-Y. Zhang, Q.-Y. Kong, N.-J. Zhao, Q. Guo, H.-L. Wu, Z.-J. Li, Y. Tao, J.-P. Zhang, B. Chen, C.-H. Tung, L.-Z. Wu, Self-assembled framework enhances electronic communication of ultrasmall-sized nanoparticles for exceptional solar hydrogen evolution, J. Am. Chem. Soc. 139 (2017) 4789–4796.

[28] Y. Shi, X.-K. Huang, Y. Wang, Y. Zhou, D.-R. Yang, F.-B. Wang, W. Gao, X.-H. Xia, Electronic metal–support interaction to modulate MoS_2-supported Pd nanoparticles for the degradation of organic dyes, ACS Appl. Nano Mater. 2 (2019) 3385–3393.

[29] J. Wang, D. Cheng, M. Gao, Q. Li, Y. Xin, N. Zhang, Z. Zhang, X. Yu, Z. Zhao, K. Zhou, Modulation of the superficial electronic structure via metal–support interaction for H_2 evolution over Pd catalysts, Chem. Sci. 12 (2021) 3245–3252.

[30] P.P. Hu, Z.W. Huang, Z. Amghouz, M. Makkee, F. Xu, F. Kapteijn, A. Dikhtiarenko, Y.X. Chen, X. Gu, X.F. Tang, Electronic metal- support interactions in single- atom catalysts, Angew. Chem. Int. Ed. 53 (2014) 3418–3421.

[31] C.T. Campbell, Electronic perturbations, Nat. Chem. 4 (2012) 597–598.

[32] N. Acerbi, S.C.E. Tsang, G. Jones, S. Golunski, P. Collier, Rationalization of interactions in precious metal/ceria catalysts using the d-band center model, Angew. Chem. Int. Ed. 52 (2013) 7737–7741.

[33] J. Yang, W. Li, D. Wang, Y. Li, Electronic metal–support interaction of single-atom catalysts and applications in electrocatalysis, Adv. Mater. 32 (2020), 2003300.

[34] F. Wang, Y. Jiang, D.J. Lawes, G.E. Ball, C. Zhou, Z. Liu, R. Amal, Analysis of the promoted activity and molecular mechanism of hydrogen production over fine Au–Pt alloyed TiO_2 photocatalysts, ACS Catal. 5 (2015) 3924–3931.

[35] A. Meng, L. Zhang, B. Cheng, J. Yu, Dual cocatalysts in TiO_2 photocatalysis, Adv. Mater. 31 (2019), 1807660.

[36] Z. Wang, L. Wang, B. Cheng, H. Yu, J. Yu, Photocatalytic H_2 evolution coupled with furfuralcohol oxidation over Pt-modified ZnCdS solid solution, Small Methods 5 (2021), 2100979.

[37] X. Xiang, B. Zhu, J. Zhang, C. Jiang, T. Chen, H. Yu, J. Yu, L. Wang, Photocatalytic H_2-production and benzyl-alcohol-oxidation mechanism over CdS using Co^{2+} as hole cocatalyst, Appl. Catal. B 324 (2023), 122301.

[38] X. He, Q. Liu, D. Xu, L. Wang, H. Tang, Plasmonic TiN nanobelts assisted broad spectrum photocatalytic H2 generation, J. Mater. Sci. Technol. 116 (2022) 1–10.

[39] X.-B. Fan, S. Yu, H.-L. Wu, Z.-J. Li, Y.-J. Gao, X.-B. Li, L.-P. Zhang, C.-H. Tung, L.-Z. Wu, Direct synthesis of sulfide capped CdS and CdS/ZnS colloidal nanocrystals for efficient hydrogen evolution under visible light irradiation, J. Mater. Chem. A 6 (2018) 16328–16332.

[40] K.P. McClelland, E.A. Weiss, Selective photocatalytic oxidation of benzyl alcohol to benzaldehyde or C–C coupled products by visible-light-absorbing quantum dots, ACS Appl. Energy Mater. 2 (2019) 92–96.

[41] N.A. Hamizi, M.R. Johan, Z.Z. Chowdhury, Y.A. Wahab, Y. Al-Douri, A.M. Saat, O. A. Pivehzhani, Raman spectroscopy and FTIR spectroscopy studies of Mn-doped CdSe QDs at different particles size, Optik 179 (2019) 628–631.

[42] X. Huang, Y. Chen, X. Feng, X. Hu, Y. Zhang, L. Liu, Incorporation of oleic acid-modified Ag@ZnO core-shell nanoparticles into thin film composite membranes for enhanced antifouling and antibacterial properties, J. Membr. Sci. 602 (2020), 117956.

[43] M.N. Kalasad, A.K. Rabinal, B.G. Mulimani, Ambient synthesis and characterization of high-quality CdSe quantum dots by an aqueous route, Langmuir 25 (2009) 12729–12735.

[44] P. Sheng, W. Li, J. Cai, X. Wang, X. Tong, Q. Cai, C.A. Grimes, A novel method for the preparation of a photocorrosion stable core/shell CdTe/CdS quantum dot TiO_2 nanotube array photoelectrode demonstrating an AM 1.5G photoconversion efficiency of 6.12%, J. Mater. Chem. A 1 (2013) 7806–7815.

[45] N. Li, Y. Ding, J. Wu, Z. Zhao, X. Li, Y. Zheng, M. Huang, X. Tao, Efficient, full spectrum-driven H_2 evolution Z-scheme Co_2P/CdS photocatalysts with Co-S bonds, ACS Appl. Mater. Interfaces 11 (2019) 22297–22306.

[46] C.P. Cullen, C.Ó. Coileáin, J.B. McManus, O. Hartwig, D. McCloskey, G. S. Duesberg, N. McEvoy, Synthesis and characterisation of thin-film platinum disulfide and platinum sulfide, Nanoscale 13 (2021) 7403–7411.

[47] S. Monaghan, E.M. Coleman, L. Ansari, J. Lin, A. Buttimer, P.A. Coleman, J. Connolly, I.M. Povey, B. Kelleher, C.Ó. Coileáin, N. McEvoy, P.K. Hurley, F. Gity, Structural and electrical characterisation of PtS from H_2S-converted Pt, Appl. Mater. Today 25 (2021), 101163.

[48] J. Guo, Y. Cao, R. Shi, G.I.N. Waterhouse, L. Wu, C. Tung, T. Zhang, A photochemical route towards metal sulfide nanosheets from layered metal thiolate complexes, Angew. Chem. Int. Ed. 58 (2019) 8443–8447.

[49] C. Cheng, B. He, J. Fan, B. Cheng, S. Cao, J. Yu, An inorganic/organic S-scheme heterojunction H_2-production photocatalyst and its charge transfer mechanism, Adv. Mater. 33 (2021), 2100317.

[50] T. Di, Q. Deng, G. Wang, S. Wang, L. Wang, Y. Ma, Photodeposition of CoO_x and MoS_2 on CdS as dual cocatalysts for photocatalytic H_2 production, J. Mater. Sci. Technol. 124 (2022) 209–216.

[51] M.-H. Sun, M.-Y. Qi, C.-L. Tan, Z.-R. Tang, Y.-J. Xu, Interfacial engineering of CdS for efficient coupling photoredox, Chin. Chem. Lett. 34 (2023), 108022.

[52] J.X. Bai, W.L. Chen, R.C. Shen, Z.M. Jiang, P. Zhang, W. Liu, X. Li, Regulating interfacial morphology and charge-carrier utilization of Ti_3C_2 modified all-sulfide $CdS/ZnIn_2S_4$ S-scheme heterojunctions for effective photocatalytic H_2 evolution, J. Mater. Sci. Technol. 112 (2022) 85–95.

[53] Z.H. Mei, G.H. Wang, S.D. Yan, J. Wang, Rapid microwave-assisted synthesis of 2D/1D $ZnIn_2S_4/TiO_2$ S-scheme heterojunction for catalyzing photocatalytic hydrogen evolution, Acta Phys. -Chim. Sin. 37 (2021), 2009097.

[54] Y.-L. Wu, M.-Y. Qi, C.-L. Tan, Z.-R. Tang, Y.-J. Xu, Photocatalytic selective oxidation of aromatic alcohols coupled with hydrogen evolution over CdS/WO_3 composites, Chin. J. Catal. 43 (2022) 1851–1859.

[55] P. Kuang, Y. Wang, B. Zhu, F. Xia, C. Tung, J. Wu, H. Chen, J. Yu, Pt single atoms supported on N-doped mesoporous hollow carbon spheres with enhanced electrocatalytic H_2-evolution activity, Adv. Mater. 33 (2021), 2008599.

[56] M. Sayed, J. Yu, G. Liu, M. Jaroniec, Non-noble plasmonic metal-based photocatalysts, Chem. Rev. 122 (2022) 10484–10537.

[57] Z. Lou, M. Fujitsuka, T. Majima, Pt–Au triangular nanoprisms with strong dipole plasmon resonance for hydrogen generation studied by single-particle spectroscopy, ACS Nano 10 (2016) 6299–6305.
[58] Y. Chen, W. Zhong, F. Chen, P. Wang, J. Fan, H. Yu, Photoinduced self-stability mechanism of CdS photocatalyst: The dependence of photocorrosion and H_2-evolution performance, J. Mater. Sci. Technol. 121 (2022) 19–27.
[59] J. Liu, Y. Liu, N. Liu, Y. Han, X. Zhang, H. Huang, Y. Lifshitz, S.-T. Lee, J. Zhong, Z. Kang, Metal-free efficient photocatalyst for stable visible water splitting via a two-electron pathway, Science 347 (2015) 970–974.
[60] Z. Li, J. Wang, X. Li, X. Fan, Q. Meng, K. Feng, B. Chen, C. Tung, L. Wu, An exceptional artificial photocatalyst, Ni_h-CdSe/CdS Core/Shell hybrid, made in situ from CdSe quantum dots and nickel salts for efficient hydrogen evolution, Adv. Mater. 25 (2013) 6613–6618.
[61] J. Zhang, G. Yang, B. He, B. Cheng, Y. Li, G. Liang, L. Wang, Electron transfer kinetics in CdS/Pt heterojunction photocatalyst during water splitting, Chin. J. Catal. 43 (2022) 2530–2538.
[62] L. Sun, L. Li, J. Fan, Q. Xu, D. Ma, Construction of highly active WO_3/TpPa-1-COF S-scheme heterojunction toward photocatalytic H_2 generation, J. Mater. Sci. Technol. 123 (2022) 41–48.
[63] C. Cheng, B. Zhu, B. Cheng, W. Macyk, L. Wang, J. Yu, Catalytic conversion of styrene to Benzaldehyde over S-scheme photocatalysts by singlet oxygen, ACS Catal. 13 (2023) 459–468.
[64] Y. Yang, J. Wu, B. Cheng, L. Zhang, A.A. Al-Ghamdi, S. Wageh, Y. Li, Enhanced photocatalytic H_2-production activity of CdS nanoflower using single atom Pt and graphene quantum dot as dual cocatalysts, Chin. J. Struct. Chem. 41 (2022) 2206006–2206014.
[65] C. Bie, B. Zhu, L. Wang, H. Yu, C. Jiang, T. Chen, J. Yu, A. Bifunctional, CdS/MoO_2/MoS_2 catalyst enhances photocatalytic H_2 evolution and pyruvic acid synthesis, Angew. Chem. Int. Ed. 61 (2022), e202212045.
[66] J. Zhang, B. Zhu, L. Zhang, J. Yu, Femtosecond transient absorption spectroscopy investigation into the electron transfer mechanism in photocatalysis, Chem. Commun. 59 (2023) 688–699.
[67] X. Guo, P. Guo, C. Wang, Y. Chen, L. Guo, Few-layer WSe_2 nanosheets as an efficient cocatalyst for improved photocatalytic hydrogen evolution over $Zn_{0.1}Cd_{0.9}S$ nanorods, Chem. Eng. J. 383 (2020), 123183.
[68] K. Wu, H. Zhu, Z. Liu, W. Rodriguez-Cordoba, T. Lian, Ultrafast charge separation and long-lived charge separated state in photocatalytic CdS–Pt nanorod heterostructures, J. Am. Chem. Soc. 134 (2012) 10337–10340.
[69] C. Cheng, J. Zhang, B. Zhu, G. Liang, L. Zhang, J. Yu, Verifying the charge-transfer mechanism in S-scheme heterojunctions using femtosecond transient absorption spectroscopy, Angew. Chem. Int. Ed. 62 (2023), e202218688.
[70] X.Y. Lu, A.M. Tong, D.A. Luo, F. Jiang, J.D. Wei, Y.C. Huang, Z. Jiang, Z. Lu, Y. H. Ni, Confining single Pt atoms from Pt clusters on multi-armed CdS for enhanced photocatalytic hydrogen evolution, J. Mater. Chem. A 10 (2022) 4594–4600.
[71] T. O'Connor, M.S. Panov, A. Mereshchenko, A.N. Tarnovsky, R. Lorek, D. Perera, G. Diederich, S. Lambright, P. Moroz, M. Zamkov, The effect of the charge-separating interface on exciton dynamics in photocatalytic colloidal heteronanocrystals, ACS Nano 6 (2012) 8156–8165.